A Switchable Mid-Infrared Plasmonic Perfect Absorber with Multispectral Thermal Imaging Capability

Andreas Tittl, Ann-Katrin U. Michel, Martin Schäferling, Xinghui Yin, Behrad Gholipour, Long Cui, Matthias Wuttig, Thomas Taubner, Frank Neubrech, and Harald Giessen*

Optical imaging devices in the mid-infrared play a key role for many technological applications in areas as diverse as thermography, surveillance, automotive safety, and astronomy. The key to this functionality are the atmospheric transmission windows in the 3–5 µm and 8–12 µm spectral ranges, which allow such devices to work without disturbance from water vapor, dust, or other atmospheric influences.[1] Traditional microbolometer arrays rely on temperature sensitive pixels combined with a broadband and passive absorbing layer to image spectrally uniform objects. However, to effectively detect and differentiate objects with distinct temperatures and corresponding peak blackbody emission wavelengths, spectrally selective absorptive coatings are needed.[2]

Here, we present the experimental demonstration of a band- and consequently temperature-selective switchable mid-infrared plasmonic perfect absorber with multispectral thermal imaging capability. The basic building blocks of our design are absorber pixels consisting of an array of square aluminum (Al) nanoantennas stacked above a $Ge_3Sb_2Te_6$ (GST-326) spacer layer and an Al mirror (**Figure 1**a). Thus, each absorber pixel is uniquely characterized by the side length d of the Al nanoantennas, which determines the resonance wavelength, and by the total size of the array, referred to as the pixel size. To achieve the switchable, band-selective performance of our design, we utilize the amorphous to crystalline phase transition in GST-326 (Figure 1b) to provide strong reflectance contrast at resonance as well as pronounced phase-change-induced spectral shifts of up to 25%.

Furthermore, by implementing pixels with spectrally distinct absorption bands on a single detector chip, our design is able to resolve several different wavelengths simultaneously, known as multispectral imaging,[3] and can be integrated on sub-10 µm pixel sizes, well below the current industrial state of the art for microbolometer pixels in the 20 µm range.[4,5]

In contrast to previous absorber designs,[6,7] we incorporate aluminum instead of gold for the metal nanostructures and mirror to obtain full compatibility with industry standard complementary metal-oxide-semiconductor (CMOS) wafer-scale processing technology, and to avoid Au-GST interdiffusion, which impedes the germanium antimony telluride (GST) phase transition in switching experiments.[8]

Compared to thin-film-based approaches,[9–11] the resonant plasmonic character of our device enables straightforward geometrical wavelength tunability by varying the antenna side length and allows our design to efficiently absorb radiation for a wide range of operating wavelengths.

In particular, we design our absorber geometry to exhibit near-perfect absorption at a given wavelength in the 3–5 µm midwave infrared (MWIR) spectral range. The MWIR plays a key role in industry, since it covers wavelengths where objects with temperatures ranging from ≈300 to 700 °C exhibit peak thermal emission. Here, each individual absorber pixel with a given resonance wavelength will most efficiently absorb radiation associated with a corresponding temperature. Integrated as the absorbing layer on top of a microbolometer geometry, this results in a spectrally selective thermal imaging device ideally suited for applications in materials science, industrial process monitoring, and exhaust tracking.

To develop an optimized device design for fabrication, we calculate the reflectance of absorber geometries with different values of the critical structure parameters antenna side length and spacer height using a scattering-matrix-based Fourier modal method[12,13] (Figure S1, Supporting Information). The results are then used to identify parameter combinations with high absorbance and suitable resonance wavelengths, which are found for an optimum GST spacer height of around 65 nm. To offset surface degradation of the GST during fabrication, a higher spacer thickness is chosen in experiment.

For a first experimental realization, we fabricate 100 µm × 100 µm absorber pixels consisting of Al nanoantenna arrays with varying antenna side lengths d, stacked above an 85 nm GST-326 spacer layer and a 100 nm Al mirror (Figure 1c). The height and periodicity of the nanoantennas are fixed at 40 nm and 800 nm, respectively, for all devices presented in this manuscript. Figure 1d depicts the reflectance from two representative absorber pixels with as-deposited GST-326 in the amorphous phase (solid lines), measured using a Fourier-Transform-Infrared (FTIR) spectrometer with attached microscope.

Our design exhibits low reflectance and hence very high absorbance in the MWIR spectral range, with a peak absorbance value of $A > 90\%$ at a wavelength of 3 µm. Furthermore, the resonance wavelength of the absorber pixels can easily be

A. Tittl, Dr. M. Schäferling, X. Yin, Dr. F. Neubrech, Prof. H. Giessen
4th Physics Institute and Research Center Scope
University of Stuttgart
D-70569 Stuttgart, Germany
E-mail: a.tittl@pi4.uni-stuttgart.de

A.-K. U. Michel, Prof. M. Wuttig, Prof. T. Taubner
I. Institute of Physics (IA)
RWTH Aachen University
D-52056 Aachen, Germany

Dr. B. Gholipour, L. Cui, Prof. H. Giessen
Centre for Disruptive Photonic Technologies
Nanyang Technological University
637371 Singapore, Singapore

DOI: 10.1002/adma.201502023

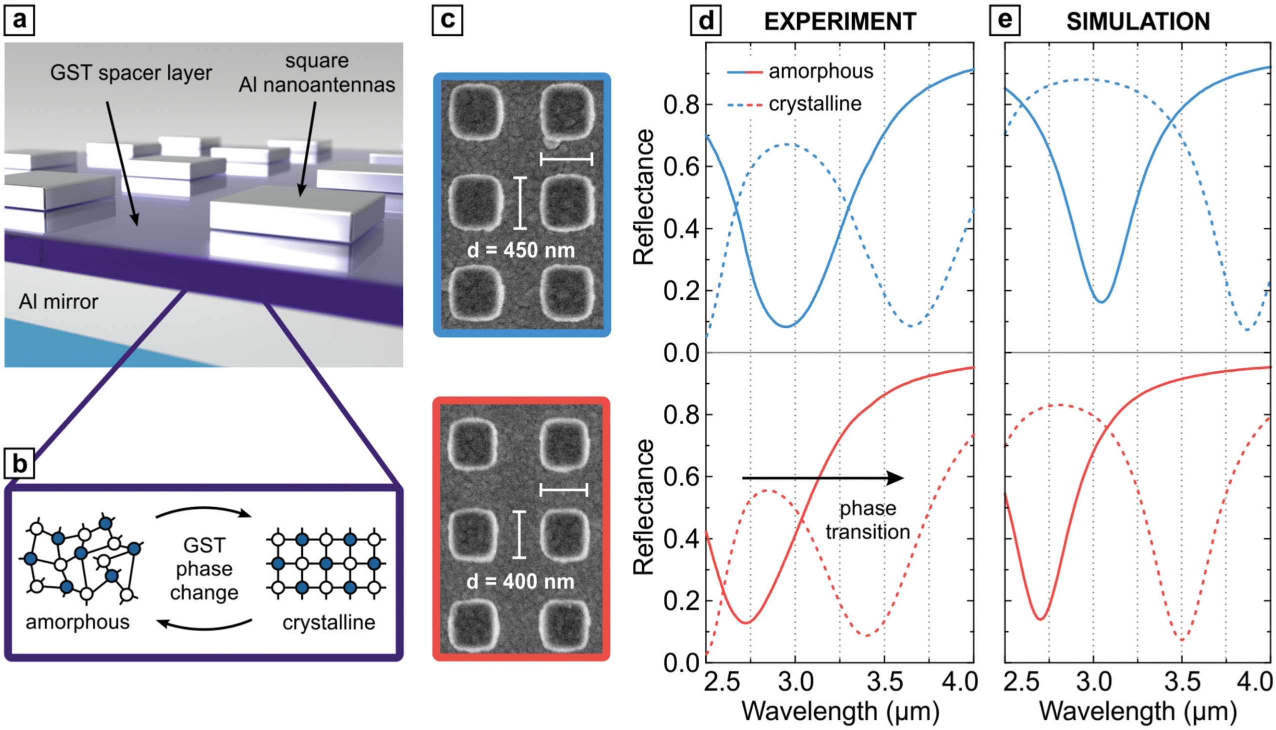

Figure 1. a) Sketch of the switchable perfect absorber device. Arrays of square aluminum (Al) nanoantennas are stacked above a spacer layer of the phase change material GST-326 and an Al mirror. b) Amorphous to crystalline phase transition in GST. c) SEM images of two representative perfect absorber devices fabricated with antenna side lengths of $d = 400$ nm and $d = 450$ nm. d) Experimental measurements show that our design exhibits low reflectance and hence very high resonant absorption ($A > 90\%$) in the MWIR spectral range. Geometrical tunability of the resonance wavelength is achieved by varying the side length d of the resonant square Al nanoantennas, with larger antennas corresponding to higher resonance wavelengths. Full tunability of the resonance over the MWIR spectral range is demonstrated in Figure 3. When heating the sample above the GST crystallization temperature, the resonance undergoes a pronounced phase-change-induced spectral redshift of up to 0.7 µm while maintaining high absorbance (dashed lines). This results in a pronounced reflectance contrast of up to $\Delta R = 0.6$ at resonance for $d = 450$ nm. e) Experimental results are in good agreement with numerical simulations on the same system.

tailored by changing the antenna side length. Importantly, our design is not limited to these wavelengths, and full geometrical tunability of the perfect absorber resonance over the whole MWIR spectral range is experimentally demonstrated in Figure 3. To obtain active control over the absorptive behavior, we induce the amorphous-to-crystalline phase transition in GST-326 by heating the sample above the phase transition temperature of 160 °C.[14] Specifically, our samples are placed on a 180 °C hot plate under nitrogen atmosphere for 30 min to avoid further heating-induced oxidation of the GST layer. When performing switching experiments in air, this effect may be avoided by covering the active material with a thin 15 nm ZnS/SiO_2 capping layer[15] without sacrificing performance (Figure S3, Supporting Information).

GST-326 is an ideal candidate for incorporation in active mid-infrared plasmonic devices due to its lower mid-infrared losses compared to more common stoichiometries.[14,16] Generally, GST compounds can be stabilized in two different phases (amorphous and crystalline) at room temperature, which show significant contrast in their optical and electrical properties.[17] This non-volatility at room temperature has been utilized extensively in rewritable optical data storage applications,[18,19] and constitutes a significant advantage over active optical devices based on vanadium dioxide,[10,11] which undergoes a semiconductor-to-metal phase transition when heated above a transition temperature of 67 °C in bulk.[20] However, since vanadium dioxide requires constant heating above the transition temperature to maintain the material in its high-temperature state, it is not well-suited for incorporation in a microbolometer-targeted absorber device.

As a further benefit, the GST phase transition is reversible and can be induced by external heating or triggered optically on nano- and possibly even picosecond timescales.[8,21–23] In recent years, these advantageous properties have enabled several active plasmonic devices based on GST.[8,14,15] Electrical switching on very fast timescales is also possible.[9,24,25]

During the phase transition, the perfect absorber resonances undergo a pronounced redshift of up to 0.7 µm, or 25% of the resonance wavelength, while maintaining high absorbance (Figure 1d, dashed lines), allowing us to switch between two spectrally distinct mid-infrared absorption bands for a single antenna length.

This pronounced optical modulation is facilitated by the strong refractive index increase of phase change materials such as GST-326 when going from the amorphous (n = 3.5) to the crystalline (n = 6.5) phase.[14,17] Because of the strong spectral shift and the low full width at half maximum (FWHM) of ≈0.5 µm, our absorber device exhibits a pronounced reflectance contrast of up to $\Delta R = 0.6$ at resonance. Compared to recent GST-based thin-film approaches,[9] our design can achieve resonant absorption with low FWHM over the full working range of the device, providing increased reflectance contrast. Additionally, the active absorption control and band-selectivity in our device represent a clear advantage over current passive mid-infrared absorber designs.[26–29]

To theoretically support the experimental switching performance, we again perform numerical calculations on the system. We find good agreement between simulation and experiment, taking into account the formation of a thin oxide layer at the surface of the GST spacer layer during fabrication[30,31] (Figure 1e; see further details in the Supporting Information).

Additionally, due to the incorporation of square nanoantennas and a low-periodicity impedance-matched design,[32] our device offers full polarization independence and high absorptive performance for incidence angles up to 65° (Figure S2, Supporting Information).

Wavelength-tunable plasmonic perfect absorber devices are commonly fabricated lithographically and feature nanostructured areas on the order of 100 µm × 100 µm. However, to enable advanced technological applications such as high-resolution imaging, plasmonic printing, color filtering, or novel displays,[33–38] current plasmonic and nanooptical designs need to be implemented for pixel sizes approaching the device operating wavelength.

To prove the viability of our design for state-of-the-art microbolometer pixel sizes in the sub-20 µm range,[39] we fabricate a checkerboard pattern composed of perfect absorber pixels with two distinct design wavelengths of $\lambda_1 = 3.4 \mu\text{m}$ and $\lambda_2 = 3.9 \mu\text{m}$ (**Figure 2**a). To achieve this dual-wavelength behavior, the individual absorber pixels incorporate arrays of square Al nanoantennas with antenna side lengths of d = 400 nm and d = 500 nm, respectively, stacked above a 75 nm GST-326 spacer layer and a 100 nm Al mirror. Due to the lower GST thickness, resonances are redshifted compared to the large pixel results from Figure 1d.

We then image this pattern using a focal plane array (FPA) detector attached to a FTIR spectrometer, allowing us to record the full spectral response of a whole pattern simultaneously (further measurement details can be found in the experimental section).

The spatially resolved reflectance at the two design wavelengths is shown in Figure 2b. At the first design wavelength ($\lambda_1 = 3.4 \mu\text{m}$), square 20 µm × 20 µm areas with low reflectance (blue color) can be clearly identified, exhibiting excellent contrast and spatial separation from adjacent areas of the pattern. When examining the reflectance at the second design wavelength ($\lambda_2 = 3.9 \mu m$), the situation is reversed, with reflective pixels at λ_1 now appearing absorptive and vice versa. This behavior is due to the high absorption of our device combined with the low FWHM of the resonances, which enables a spectrally non-overlapping pixelated absorber design. For a more challenging design with 10 µm pixel size, individual pixels in the checkerboard pattern are still clearly visible with high contrast and good spatial separation (Figure 2c).

When reducing the pixel size to 5 µm, which is on the order of the device operating wavelength, the reflectance contrast at the two design wavelengths is decreased. However, individual pixels containing only 6 × 6 Al nanoantennas can still be clearly distinguished (Figure 2d). Importantly, this pixel size is close to the diffraction limit of mid-infrared radiation and approaches the ultimate limit of a single resonant nanostructure pixel.

Building on this two-wavelength design, we now extend our perfect absorber device toward multiband operation in the mid-infrared, allowing for the simultaneous implementation of several distinct absorption bands similar to the RGB (red

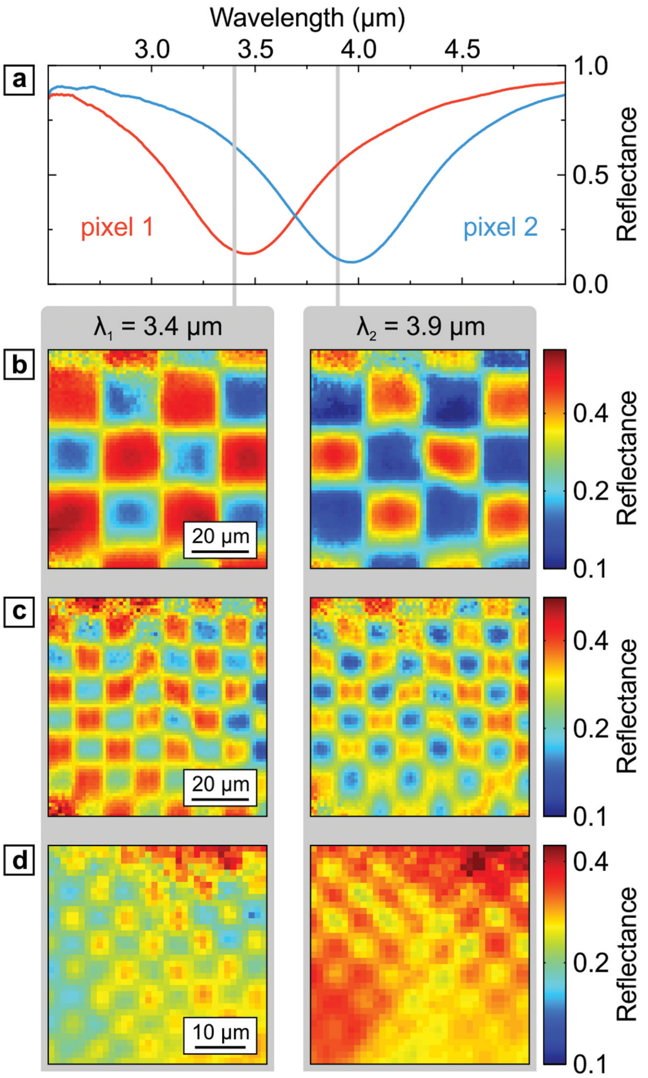

Figure 2. Spatially resolved reflectance of perfect absorber geometries consisting of a checkerboard pattern of absorber pixels with two different design wavelengths (3.4 and 3.9 µm). Reflectance data are recorded using a focal-plane array (FPA) detector connected to an FTIR spectrometer. a) Representative reflectance spectra for the two pixels. b) Color-coded reflectance at the design wavelengths of the two distinct perfect absorber pixels for a pixel size of 20 µm. The pixel arrangement can be clearly distinguished. c) Perfect absorber pixels with 10 µm size. The regular arrangement is again neatly visible. d) Perfect absorber pixels with 5 µm size on the order of the device operating wavelength. Even though contrast is reduced, individual pixels can still be clearly distinguished. A logarithmic reflectance scale is used in panels (b)–(d). Please note the smaller scale bar in panel (d). The GST spacer layer is in the amorphous phase for all measurements.

green blue) color filter arrays in digital camera sensor chips. To achieve this, we utilize a conceptual advantage of our design: the ability to obtain near-perfect wavelength-tunable absorption for different nanoantenna side lengths on a single GST spacer layer thickness (Figure S1, Supporting Information). This enables pixelated patterns with a wide range of different operating wavelengths on a single integrated infrared absorber chip, also known as multispectral imaging.

In recent years, this concept has increasingly been applied in plasmonics, with multiband mid-infrared absorbers being realized using spatial multiplexing[40] or double-resonant nanoantennas.[41] With more complex designs, co-integrated absorption of wavelength bands with large spectral separation, notably of terahertz and visible/mid-infrared radiation, can also be achieved.[42–44]

In our case, we realize this multispectral concept experimentally by fabricating a perfect absorber device with a periodic superpixel arrangement composed of four individual pixels with distinct resonance wavelengths in the 2.5–4 µm range. The design integrates Al nanoantenna arrays with side lengths ranging from 300 to 450 nm in 50 nm steps, stacked above a 75 nm GST-326 spacer layer and a 100 nm Al mirror (Figure S4, Supporting Information).

To further elucidate the multispectral operation of the superpixel geometry, we extract the wavelength of lowest reflectance (resonance wavelength) from spatially resolved FTIR measurements on this pattern (**Figure** 3a). The four different design wavelengths are clearly visible with excellent spatial and spectral separation. Additionally, representative reflectance spectra from the four individual pixels clearly demonstrate the high absorptive performance (A > 80%) and non-overlapping spectral characteristics of our design even for multiple mid-infrared absorption bands (Figure 3b–e).

In addition to the multispectral capability, which allows to resolve multiple wavelengths of incident radiation on a single integrated detector chip, the use of GST in our design adds postfabrication band-selectivity. This active switching of individual absorber pixels does not reduce the final resolution of the microbolometer detector chip, resulting in a more versatile device.

Previous studies on GST-based active plasmonic devices have commonly focused on switching between its two nonvolatile amorphous and crystalline phases.[14,15,45] This bistability is a key differentiating factor of phase change materials, but may limit the realization of continuously tunable nanophotonic devices. However, it has recently been shown that GST-225 can be prepared in intermediate crystallization states by time-controlled external heating[46] or focused femtosecond laser pulses.[47] Due to the physical similarity between the two stoichiometries, such intermediate states are likely to be realized for GST-326 in the future.

For further validation of the thermal imaging capability of our absorber device, we now relate the spectral locations of the four mid-infrared absorption bands (**Figure** 4a) to the peak emission wavelength of an ideal blackbody with a specific temperature via Planck's law. That is, for every resonance wavelength, thermal emission from a heated object with this specific temperature is absorbed most efficiently (Figure 4b). In the following, this calculated "peak detection temperature" is used to characterize the thermal detection range and temperature-selective operation of our design.

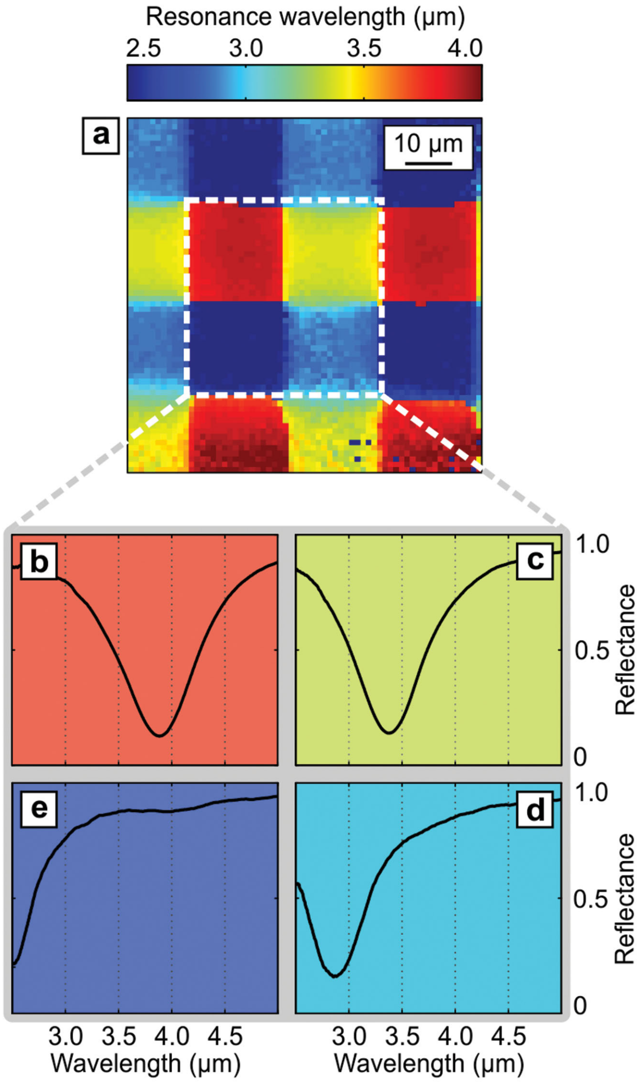

Figure 3. a) Color-coded resonance wavelength of a four-wavelength pixelated plasmonic perfect absorber chip for multispectral imaging. Our device covers a wavelength range from 2.5 to 4 µm. This is achieved using Al nanoantenna arrays with antenna side lengths varying from 300 to 450 nm in 50 nm steps. The four individual pixels in the superpixel arrangement (white square) deliver a peak absorbance of $A > 80\%$ at resonance while providing 20 µm pixel size. b–d) Representative reflectance spectra for the individual pixels. The resonance wavelength in panel (a) is taken as the reflectance minimum in the spectral range from 2.5 to 5 µm. The GST spacer layer is in the amorphous phase for all measurements.

Focusing on an individual superpixel, we find multispectral thermal imaging capability for peak detection temperatures ranging from 740 to 1150 K (Figure 4c). Importantly, when thermal radiation of a blackbody with a certain temperature impinges on this geometry, the individual pixels absorb different amounts of radiation due to their spectrally distinct absorption bands. Especially, the pixel closest in wavelength to the thermal emission peak will absorb the largest amount of incident energy, resulting in maximum local heat generation.

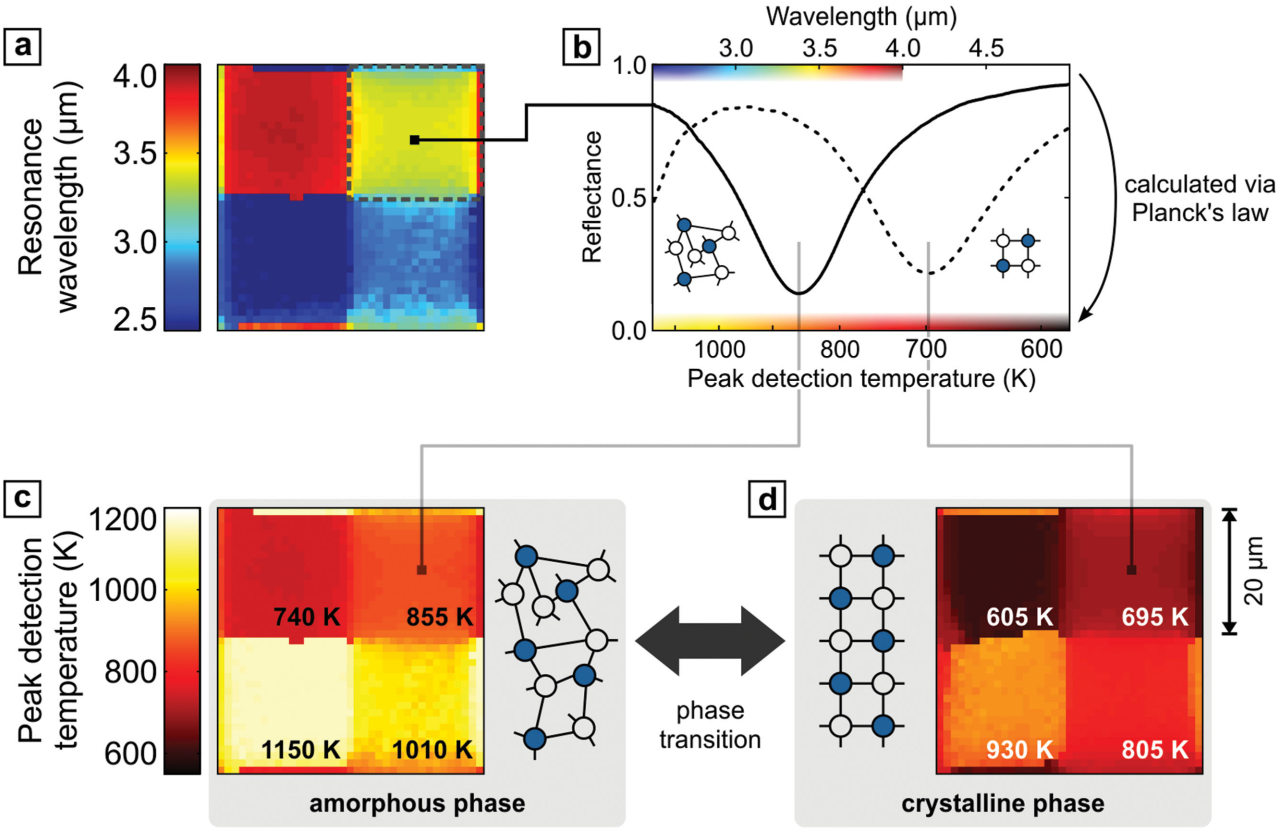

Figure 4. a) Color-coded resonance wavelength of an individual perfect absorber superpixel with four distinct mid-infrared absorption bands. b) Representative reflectance spectra for the top right pixel from panel (a) with the GST-326 layer in the amorphous (solid line) and crystalline phase (dashed line). The peak detection temperature is calculated from the resonance wavelength of the perfect absorber pixels using Planck's law. c) Color-coded peak detection temperature for the multispectral superpixel geometry. Our device offers multispectral thermal imaging capability for temperatures ranging from 740 to 1150 K. The numerical overlay in the lower right corner of each individual pixel represents the average peak detection temperature for this pixel. d) Color-coded peak detection temperature after heat-induced phase change of the GST layer from the amorphous to the crystalline phase. The multispectral imaging capability is maintained and shifted to the temperature range from 605 to 930 K. Pixel size is 20 µm for all pixels shown in panels (a), (c), and (d).

For a second blackbody temperature, thermal emission peaks at a different wavelength, leading to a redistribution of heat over the four absorber pixels. The local temperature changes associated with this process can be resolved using an adjacent microbolometer array, allowing our superpixel design to easily differentiate objects with different temperatures (Figure S5, Supporting Information).

Building on this, the range of detection temperatures can now be tailored by utilizing the reversible amorphous to crystalline phase transition in GST. When heating the sample above the transition temperature, the multispectral thermal imaging capability is maintained and undergoes a shift to the temperature range from 605 to 930 K (Figure 4d), again with high absorptive performance ($A > 75\%$) and spectrally distinct absorption bands (Figure S6, Supporting Information). Thus, our versatile thermal imaging chip offers the ability to actively switch between different temperature detection ranges, enabling applications such as selective thermography and chemical imaging. Due to the wavelength tunability of our design, other temperature ranges can be implemented easily, enabling the straightforward realization of thermal imaging in the 8–12 µm spectral window.

As a first demonstration of switching in a multispectral mid-infrared perfect absorber, our device utilizes the heat-induced phase change of a GST-326 spacer layer. However, due to the robust material and phase change properties of our design, reversible optical switching should be possible as recently shown for Al nanoantenna arrays covered with a thin GST-326 film.[8] If necessary, the optical accessibility of the phase change material in our design can be optimized further by utilizing fully GST-covered Al antennas placed on a CMOS compatible dielectric spacer layer.

In order to obtain full electrical control of the absorption, our design can be extended to incorporate nanostructured and individually contacted Al/GST nanostacks (Figure S7, Supporting Information). By applying a voltage pulse to individual nanostacks, reversible electrical switching of the nanostructured GST can be carried out.[9] Electrical switching, especially on fast timescales, may also be useful for background-correction and lock-in detection approaches.

Moving closer to the technological realization of multispectral switchable microbolometer devices, future studies will need to focus on heat generation and transfer in plasmonic absorption layers,[48,49] optimizing them for high sensitivity and low response times. In particular, lateral heat diffusion, which decreases microbolometer resolution, can be reduced by subdividing the continuous Al mirror into discreet Al patches separated by dielectric gaps without reducing absorption or dynamic range (Figure S8, Supporting Information). Due to the high volumetric heat capacity of aluminum, it may also be necessary to decrease the amount of Al in the design to reach low microbolometer response times. This can be achieved by reducing the thickness of the Al mirror and nanoantennas without degradation of the optical performance (Figure S9, Supporting Information).

In conclusion, we have presented the first experimental demonstration of a band- and consequently temperature-selective switchable mid-infrared perfect absorber with multispectral thermal imaging capability. Our design exhibits high absorptive performance independent of incident angle and polarization and can be integrated in sub-10 µm absorber pixels, which allows for near diffraction-limited imaging in the mid-infrared. The near-perfect ($A > 90\%$) absorption in our design combined with the use of a GST-326 spacer layer enables efficient band- and thus temperature-selective detection. By simultaneously increasing the number of pixels and reducing the FWHM of the resonances in our multispectral design, more wavelengths can be resolved simultaneously, paving the way toward advanced imaging applications in meteorology, geoscience, or defence. Integrating the possibility of switching the GST-326 layer using all-optical or electrical means, our perfect absorber design can serve as a building block for highly selective absorptive coatings with ultrafast control and a wide range of design wavelengths in the future.

Experimental Section

Sample Fabrication: The perfect absorber samples were fabricated using electron-beam lithography and wet-chemical lift-off. Clean silicon substrates were covered with the Al mirror and GST-326 spacer layer via sputtering and co-sputtering, respectively. The GST-326 film has been deposited by direct current magnetron sputtering with a background pressure of 2×10^{-6} mbar and 20 sccm Ar flow. Afterward, the nanoantenna geometry was defined in poly(methyl methacrylate) (PMMA) resist using an electron-beam lithography step. Al was then deposited into the PMMA mask using electron-beam-assisted evaporation. Finally, the PMMA mask was removed in *n*-ethyl-2-pyrrolidone (NEP) to yield the complete device.

Infrared Focal Plane Array Measurements: Spectroscopic infrared imaging of our perfect absorber devices (Figures 2–4) was carried out with an IR microscope (Bruker Hyperion 1000) connected to a Fourier-Transform-Infrared (FTIR) spectrometer (Bruker IFS 66v/S) at the synchrotron light source ANKA (Angstrom Source Karlsruhe). The described measurements were done with a globar to ensure a uniform illumination of the sample. The IR microscope was equipped with a liquid nitrogen-cooled mercury cadmium telluride focal plane array (FPA) detector consisting of 64×64 elements with 40 µm pixel pitch. A 36× magnification Schwarzschild-objective (NA = 0.52) was used to project a pixel size of 1.1 µm in the focal plane, combined with a total field of view of 71 µm × 71 µm. Please note that due to the Schwarzschild optics, aberration effects may limit the theoretical resolution given by $\lambda/(2\mathrm{NA})$. A detailed characterization of the imaging setup is provided in the literature.[50] Reflectance spectra of our perfect absorber design and a bare gold mirror were acquired between 2.5 and 12.5 µm with a resolution of 8 cm^{-1} and a minimum of 100 scans. After data smoothing (a moving average Savitzky–Golay filter with a data point span of 40 and polynomial degree 2), the relative reflection is calculated and normalized in the range of 7–7.5 µm to account for the different sensitivities of each pixel. Conventional infrared spectroscopic measurements as presented in Figure 1 were recorded with a single element detector in our labs as described previously.[51]

Supporting Information

Supporting Information is available from the Wiley Online Library or from the author.

Acknowledgements

The authors would like to thank the Max Planck Institute for Solid State Research, in particular J. Weis and T. Reindl for cleanroom access and helpful discussions; to T. Weiss for help with the numerical simulations; and to N. Strohfeldt for key advice and discussions. The authors acknowledge the synchrotron light source ANKA for provision of instruments at the IR2 beamline and would like to thank D. Moss, Y.-L. Mathis, and M. Süpfle for their assistance. The authors also thank C. Huck for help with the measurements. A.T., M.S., X.Y., F.N., and H.G. were financially supported by the Deutsche Forschungsgemeinschaft (SPP1391, FOR730, GI 269/11-1), the Bundesministerium für Bildung und Forschung (13N9048 and 13N10146), the ERC Advanced Grant COMPLEXPLAS, the Baden-Württemberg Stiftung (Spitzenforschung II, Proteinsens), and the Ministerium für Wissenschaft, Forschung und Kunst Baden-Württemberg (Az: 7533-7-11.6-8). A.-K.M., T.T., and M.W. gratefully acknowledge support within SFB 917 ("Nanoswitches"). X.Y. would like to acknowledge financial support by the Carl-Zeiss-Foundation.

Received: April 27, 2015

---

[1] S. Law, V. Podolskiy, D. Wasserman, *Nanophotonics* **2013**, *2*, 103.
[2] J. J. Talghader, A. S. Gawarikar, R. P. Shea, *Light Sci. Appl.* **2012**, *1*, e24.
[3] C. D. Tran, *Appl. Spectrosc. Rev.* **2003**, *38*, 133.
[4] T. Schimert, C. Hanson, J. Brady, T. Fagan, M. Taylor, W. McCardel, R. Gooch, M. Gohlke, A. J. Syllaios, *Proc. SPIE* **2009**, *7298*, 72980T.
[5] F. Niklaus, C. Vieider, H. Jakobsen, *Proc. SPIE* **2008**, *6836*, 68360D.
[6] T. Cao, C.-W. Wei, R. E. Simpson, L. Zhang, M. J. Cryan, *Sci. Rep.* **2014**, *4*, 3955.
[7] T. Cao, L. Zhang, R. E. Simpson, M. J. Cryan, *J. Opt. Soc. Am. B* **2013**, *30*, 1580.
[8] A.-K. U. Michel, P. Zalden, D. N. Chigrin, M. Wuttig, A. M. Lindenberg, T. Taubner, *ACS Photonics* **2014**, *1*, 833.
[9] P. Hosseini, C. D. Wright, H. Bhaskaran, *Nature* **2014**, *511*, 206.
[10] M. A. Kats, D. Sharma, J. Lin, P. Genevet, R. Blanchard, Z. Yang, M. M. Qazilbash, D. N. Basov, S. Ramanathan, F. Capasso, *Appl. Phys. Lett.* **2012**, *101*, 221101.
[11] M. A. Kats, R. Blanchard, S. Zhang, P. Genevet, C. Ko, S. Ramanathan, F. Capasso, *Phys. Rev. X* **2013**, *3*, 041004.
[12] T. Weiss, N. A. Gippius, S. Tikhodeev, G. Granet, H. Giessen, *J. Opt. A* **2009**, *11*, 114019.
[13] T. Weiss, G. Granet, N. A. Gippius, S. Tikhodeev, H. Giessen, *Opt. Express* **2009**, *17*, 8051.
[14] A.-K. U. Michel, D. N. Chigrin, T. W. W. Maß, K. Schönauer, M. Salinga, M. Wuttig, T. Taubner, *Nano Lett.* **2013**, *13*, 3470.
[15] B. Gholipour, J. Zhang, K. F. MacDonald, D. W. Hewak, N. I. Zheludev, *Adv. Mater.* **2013**, *25*, 3050.
[16] T. Siegrist, P. Jost, H. Volker, M. Woda, P. Merkelbach, C. Schlockermann, M. Wuttig, *Nat. Mater.* **2011**, *10*, 202.

[17] K. Shportko, S. Kremers, M. Woda, D. Lencer, J. Robertson, M. Wuttig, *Nat. Mater.* **2008**, *7*, 653.
[18] M. Wuttig, N. Yamada, *Nat. Mater.* **2007**, *6*, 824.
[19] T. Tsafack, E. Piccinini, B.-S. Lee, E. Pop, M. Rudan, *J. Appl. Phys.* **2011**, *110*, 063716.
[20] D. Y. Lei, K. Appavoo, Y. Sonnefraud, R. F. Haglund, S. A. Maier, *Opt. Lett.* **2010**, *35*, 3988.
[21] T. Cao, C. Wei, R. E. Simpson, L. Zhang, M. J. Cryan, *Opt. Mater. Express* **2013**, *3*, 1101.
[22] R. L. Cotton, J. Siegel, *J. Appl. Phys.* **2012**, *112*, 3520.
[23] K. Sokolowski-Tinten, J. Solis, J. Bialkowski, J. Siegel, C. N. Afonso, D. von der Linde, *Phys. Rev. Lett.* **1998**, *81*, 3679.
[24] D. Loke, T. H. Lee, W. J. Wang, L. P. Shi, R. Zhao, Y. C. Yeo, T. C. Chong, S. R. Elliott, *Science* **2012**, *336*, 1566.
[25] G. Bruns, P. Merkelbach, C. Schlockermann, M. Salinga, M. Wuttig, T. D. Happ, J. B. Philipp, M. Kund, *Appl. Phys. Lett.* **2009**, *95*, 043108.
[26] T. Maier, H. Brueckl, *Opt. Lett.* **2010**, *35*, 3766.
[27] T. Maier, H. Brueckl, *Opt. Lett.* **2009**, *34*, 3012.
[28] W. Ma, Y. Wen, X. Yu, *Opt. Express* **2013**, *21*, 30724.
[29] F. B. P. Niesler, J. K. Gansel, S. Fischbach, M. Wegener, *Appl. Phys. Lett.* **2012**, *100*, 203508.
[30] J. W. Fleming, *Appl. Opt.* **1984**, *23*, 4486.
[31] E. Gourvest, B. Pelissier, C. Vallee, A. Roule, S. Lhostis, S. Maitrejean, *J. Electrochem. Soc.* **2012**, *159*, H373.
[32] A. Tittl, M. G. Harats, R. Walter, X. Yin, M. Schäferling, N. Liu, R. Rapaport, H. Giessen, *ACS Nano* **2014**, *8*, 10885.
[33] S. J. Tan, L. Zhang, D. Zhu, X. M. Goh, Y. M. Wang, K. Kumar, C.-W. Qiu, J. K. W. Yang, *Nano Lett.* **2014**, *14*, 4023.
[34] S. Yokogawa, S. P. Burgos, H. A. Atwater, *Nano Lett.* **2012**, *12*, 4349.
[35] Q. Chen, D. R. S. Cumming, *Opt. Express* **2010**, *18*, 14056.
[36] T. Xu, Y.-K. Wu, X. Luo, L. J. Guo, *Nat. Commun.* **2010**, *1*, 1.
[37] Y. S. Do, J. H. Park, B. Y. Hwang, S.-M. Lee, B.-K. Ju, K. C. Choi, *Adv. Opt. Mater.* **2013**, *1*, 133.
[38] Q. Chen, D. Chitnis, K. Walls, T. D. Drysdale, S. Collins, D. R. S. Cumming, *IEEE Photonics Technol. Lett.* **2012**, *24*, 197.
[39] J.-L. Tissot, S. Tinnes, A. Durand, C. Minassian, P. Robert, M. Vilain, J.-J. Yon, *Opt. Eng.* **2011**, *50*, 061006.
[40] B. Zhang, J. Hendrickson, J. Guo, *J. Opt. Soc. Am. B* **2013**, *30*, 656.
[41] K. Chen, R. Adato, H. Altug, *ACS Nano* **2012**, *6*, 7998.
[42] I. J. H. McCrindle, J. Grant, T. D. Drysdale, D. R. S. Cumming, *Adv. Opt. Mater.* **2013**, *2*, 149.
[43] J. Grant, I. J. H. McCrindle, C. Li, D. R. S. Cumming, *Opt. Lett.* **2014**, *39*, 1227.
[44] H. Kang, H. Jung, H. Lee, *Adv. Opt. Mater.* **2015**, DOI: 10.1002/adom.201400622.
[45] Z. L. Sámson, S.-C. Yen, K. F. MacDonald, K. Knight, S. Li, D. W. Hewak, D. P. Tsai, N. I. Zheludev, *Phys. Status Solidi RRL* **2010**, *4*, 274.
[46] Y. G. Chen, T. S. Kao, B. Ng, X. Li, X. G. Luo, B. Luk'yanchuk, S. A. Maier, M. H. Hong, *Opt. Express* **2013**, *21*, 13691.
[47] Q. Wang, J. Maddock, E. T. F. Rogers, T. Roy, C. Craig, K. F. Macdonald, D. W. Hewak, N. I. Zheludev, *Appl. Phys. Lett.* **2014**, *104*, 121105.
[48] J. Hao, L. Zhou, M. Qiu, *Phys. Rev. B* **2011**, *83*, 165107.
[49] W. Withayachumnankul, C. M. Shah, C. Fumeaux, B. S. Y. Ung, W. J. Padilla, M. Bhaskaran, D. Abbott, S. Sriram, *ACS Photonics* **2014**, *1*, 625.
[50] D. Moss, B. Gasharova, Y.-L. Mathis, *Infrared Phys. Technol.* **2006**, *49*, 53.
[51] S. Cataldo, J. Zhao, F. Neubrech, B. Frank, C. Zhang, P. V. Braun, H. Giessen, *ACS Nano* **2012**, *6*, 979.